J. Mech. Phys. Solids 202 (2025) 106172

Contents lists available at ScienceDirect

Journal of the Mechanics and Physics of Solids

journal homepage: www.elsevier.com/locate/jmps

# Shear-lag model of laminated films with alternating stiff and soft layers wrinkling on soft substrates

Zheliang Wang [a,1], Xinyi Lin [b,1], Jia Liu [b,*], Nanshu Lu [a,*]

[a] Department of Aerospace Engineering and Engineering Mechanics, The University of Texas at Austin, TX, 78712, United States
[b] John A. Paulson School of Engineering and Applied Sciences, Harvard University, MA, 02134, United States

ARTICLE INFO

*Keywords:*
Flexible electronics
Wrinkle
Shear-lag
Flexural rigidity
Multilayer beam
Elasticity

ABSTRACT

Multilayer laminated films, consisting of alternating stiff and soft layers, are widely used in flexible electronics and photonics. The extreme modulus mismatch between these layers can induce shear-lag effects, leading to mechanical behavior distinct from conventional Euler–Bernoulli beam theory. Compared to three-point bending, wrinkling on a soft substrate is an easier-to-implement approach for probing the elasticity of ultrathin films. In this work, we introduce a wrinkle-based metrology for directly measuring the equivalent flexural rigidity of laminated beams with shear-lag. An analytical framework is developed, demonstrating good agreement with experimental results. We systematically investigate the effects of the number of layers and layer properties within the film, and substrate modulus. Additionally, we propose a criterion to determine when the wrinkle-based metrology is more suitable than the traditional three-point bending test.

## 1. Introduction

Flexible electronics have revolutionized a wide array of applications, including flexible displays (Zhao et al., 2022), flexible sensors (Luo et al., 2023) and actuators (Hui et al., 2023), wearable and implantable electronics (Sunwoo et al., 2021; Liu et al., 2022; Song et al., 2019), bio-mimetic electronic skins (Yang et al., 2019), bionic eyes (Lee et al., 2018), energy harvesting and storage devices (Vallem et al., 2021; He et al., 2024), and soft photonics (Geiger et al., 2020). Multilayer structures with alternating stiff functional layers and soft electrically insulating or mechanically isolating layers are widely adopted in numerous devices, including flexible neural interfaces (Le Floch et al., 2024), flexible battery arrays (Li et al., 2022), flexible photonics (Li et al., 2014), and flexible energy harvester (Su et al., 2015). Achieving low bending stiffness $K$ or flexural rigidity $D$ is a key objective in the development of flexible electronics. In this article, we differentiate the two as follows. $K$ is the ratio of applied force to maximum deflection, which is a global structural property that depends on the loading condition, the types of supports, and the length of the beam. $D$ is the ratio of internal moment to curvature, which is only dependent on cross-sectional properties in classic beam theory. Reduced flexural rigidity enhances the conformability of these devices (Wang and Lu, 2016; Li et al., 2024), improving their ability to maintain intimate contact with target surfaces. For wearable electronics, an increase in conformability can lead to higher signal-to-noise ratios in epidermal electrophysiological sensors and improve thermal efficiency in wearable heaters (Jang et al., 2022; Mazzotta et al., 2021). For implantable devices, minimizing flexural rigidity reduces the mechanical mismatch between devices and human tissue, reducing immune responses, and promoting long-term stability of the devices (Le Floch et al., 2024).

* Corresponding authors.
*E-mail addresses:* jia_liu@seas.harvard.edu (J. Liu), nanshulu@utexas.edu (N. Lu).
[1] Co-first authors.

https://doi.org/10.1016/j.jmps.2025.106172
Received 31 January 2025; Received in revised form 24 April 2025; Accepted 24 April 2025
Available online 15 May 2025

Euler–Bernoulli beam theory has been widely used to calculate the flexural rigidity of multilayered devices (Le Floch et al., 2024; Uzun et al., 2016; Kim et al., 2010). However, when there is orders of magnitude modulus mismatch between the soft and stiff layers, shear-lag effects kick in, leading to mechanical behavior that deviates from Euler–Bernoulli predictions (Li et al., 2014, 2016; Wang et al., 2024a). In general, shear-lag refers to cases where increased shear deformability leads to higher compliance of materials or structures under tension or bending, as observed in wide-flange beams, fiber-reinforced composites, and nacre-like materials (Reissner, 1946; Cox, 1952; Gao and Li, 2005). In multilayer laminated beams with extreme modulus mismatch, the soft layers undergo significant shear deformation, reducing axial membrane strains in the stiff layers and resulting in a lower overall effective flexural rigidity. Past shear-lag models for multilayer beams focused on estimating the strain in the stiff layers. Li et al. (2014) pioneered the exploration of shear-lag effects in flexible photonics, introducing the concept 'split of the neutral axis' after discovering that an SU8-silicone-polyimide laminate had two mechanical neutral axes. They proposed an analytical method based on force balance, using one fitting parameter derived from finite element analysis (FEA). This discovery was later validated by Lee et al. (2019) using digital image correlation to measure the full-field deformation of multilayer laminated beams. Shi et al. (2014) proposed an energy-based analytical framework without any fitting parameters. Su et al. (2015) were the first to propose that the soft layers in multilayer laminated beams act as shear-lags, incorporating the shear energy of the soft layers into their analysis. Their framework has since been successfully applied to other deformation modes and device configurations (Li et al., 2017, 2022, 2016). Recently, we expanded Su et al.'s theory (Su et al., 2015) to account for arbitrary layer numbers under various loading conditions (Wang et al., 2024a). We identified a dimensionless shear-lag number that quantifies the deviation of shear-lag theory from Euler–Bernoulli beam theory. Notably, similar analytical frameworks have also been proposed for 2D materials and nacre-like composites (Huang et al., 2023; Liu et al.; Chen et al., 2023).

Although our model (Wang et al., 2024a) offers analytical solutions for computing the flexural rigidity of multilayered beams, experimental measurement of flexural rigidity remains a challenge for highly compliant flexible electronics. Three-point bending tests are the standard method for measuring beam flexural rigidity (Standard and Iso, 2019; Standard, 1997). However, many flexible electronics are ultrathin or extremely compliant and cannot self-support (Fig. 1), causing problems both in the execution of these tests and in the interpretation of the results, as will be discussed in the Discussion section of this paper. Many methods that have been developed to characterize the elastic modulus of thin films can be adapted to measure flexural rigidity, as long as bending is the primary mode of deformation during testing. For example, the drumhead indentation test (Maner et al., 2004; Begley and Mackin, 2004), widely used to characterize thin films including 2D materials, involves indenting the center of a thin film suspended over a circular hole. This method demands careful sample preparation and a high-resolution load cell. Additionally, data analysis can be complex due to the presence of membrane forces and potential sliding at the boundaries (Rao and Lu, 2024). Similarly, the bulge test is a common method for measuring the elastic properties of thin films by applying uniform pressure to induce deflection in a suspended film (Vlassak and Nix, 1992; Xiang et al., 2005; Beams, 1959). It provides rich information, including modulus, Poisson's ratio, residual stresses and material hardening, but the control of loading and interpretation of data can be complex (Hemker and Sharpe Jr., 2007). Other methods, including micro-scale cantilever tests (Haque and Saif, 2003) and vibrational methods (Whiting and Angadi, 1990), also require specific equipment. Recently, several elastocapillary-based methods have been proposed that eliminate the need for micro-loading apparatus, but they either require repetitive experiments or are not directly suitable for measuring flexural rigidity (Bae et al., 2015; Wang et al., 2024b).

Compared to the methods mentioned above, thin film wrinkling on soft substrates stands out as a promising alternative approach to determine thin film flexural rigidity due to its simplicity to implement and straightforward data processing (Chung et al., 2011; Stafford et al., 2004). In a wrinkle test, a thin film bonded to a soft substrate forms a periodic wrinkle pattern under compression, with the wavelength and amplitude of the wrinkles related to the film's elasticity. Although commonly used to determine the elastic modulus, the wrinkling wavelength is governed by the minimization of bending energy in the film and elastic energy in the substrate, thereby reflecting the bending properties. Thin film wrinkling on soft substrates has been extensively studied analytically, numerically, and experimentally (Huang et al., 2005; Groenewold, 2001; Song et al., 2008), but the wrinkling behavior of laminated films with shear-lag effects remains unexplored. In this work, we integrate our analytical framework developed previously for laminated beams with shear-lag effects subjected to bending (Wang et al., 2024a) with the classic wrinkling theory (Groenewold, 2001; Huang et al., 2005) to unveil the wrinkle of laminated beams with shear-lag effects. An equivalent flexural rigidity is defined and related to the wavelength of the wrinkle. Experimental results are presented to validate our theoretical predictions. Although motivated by flexible electronics, the theoretical framework and metrology platform presented may also find applications in a wide range of layered nanomaterials, composites, and structural systems that exhibit large modulus mismatch or weak interfacial bonding between layers with slight modifications. Representative examples include multilayer 2D materials (Chen et al., 2019), 2D superlattice structures (Zhang et al., 2022; Xiong et al., 2020), and nacre-inspired composites (Zhao et al., 2018).

The remainder of the paper is organized as follows. Section 2 is the Methods section that outlines the experimental procedure and theoretical framework. Section 3 presents the results of the wrinkle analysis of laminated beams with shear-lag, including a systematic parameter study. Section 4 discusses the relative contributions of different energies, compares shear-lag theory with other beam theories, and contrasts the wrinkling method with the traditional three-point bending test. Finally, Section 5 provides concluding remarks.

## 2. Method

### 2.1. Experimental methods

#### 2.1.1. Sample preparation

The fabrication process of the multi-layer structure is executed in accordance with the sequential procedure depicted in the upper half of Fig. 2A:

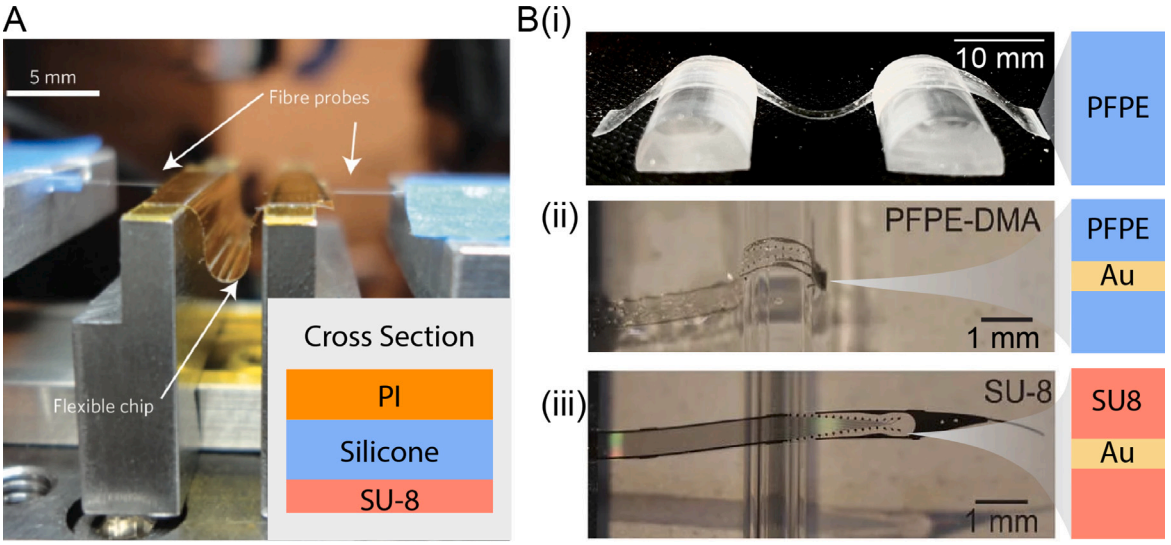


**Fig. 1.** (A) An SU-8/Silicone/Polyimide(PI) multilayer with embedded glass photonics buckles under compression. (B) (i) A 9-μm-thin dummy soft neural probe made of perfluoropolyether-dimethacrylate (PFPE-DMA) is unable to self-support and sags when placed on a simple support. (ii) A 9-μm-thin, 500-μm-wide soft PFPE-DMA neural probe embedded with a 140-nm-thin Au layer in the middle wrapping around a 1-mm-diameter glass tube due to self-weight and capillary forces (Le Floch et al., 2024). (iii) A 9-μm-thin SU-8-based neural probes embedded with a 140-nm-thin Au layer in the middle does not wrap around a 1-mm-diameter glass despite self-weight and capillary forces (Le Floch et al., 2024).

(1) A 4-inch silicon wafer is cleaned by immersing it in acetone with ultrasound for 5 min, followed by immersion in isopropanol with ultrasound for an additional 5 min, and then blown dry. A dextran sacrificial layer with a concentration of 10 wt% is uniformly applied onto the meticulously cleaned silicon wafer through spin-coating. The initial spin-coating rotational speed is set at 500 rpm/min for a duration of 5 s, followed by a subsequent speed of 4000 rpm/min sustained for 30 s. The treated wafer is subsequently subjected to thermal treatment on a hotplate maintained at 90 °C for a duration of 1 h.

(2) SU-8 2002 is spin-coated onto the treated wafer with a rotational speed of 500 rpm for 5 s, followed by a speed of 3000 rpm for 30 s. The wafer is then exposed to thermal treatment on a hotplate set at 180 °C for a duration of 1 h.

(3) A polydimethylsiloxane (PDMS) mixture, prepared in a base-agent ratio of 10:1, is subjected to spin-coating onto the wafer at a rotational speed of 500 rpm for a duration of 10 s. Subsequently, the wafer is exposed to varying spin-coating speeds for 5 min to obtain different PDMS thickness, as shown in Fig. 2D. Following this, the wafer undergoes a thermal treatment on a hotplate set at 150 °C for a duration of 1 h. To achieve a thickness of the PDMS below 1 μm, hexane is introduced into the PDMS mixture in various mass ratios, as elucidated in Fig. 2E. The hexane/PDMS mixture is then gently applied onto the wafer through spin-coating, with a spin-coating speed of 500 rpm for 10 s and subsequently employing differing spin-coating speeds for 1 min, tailored to produce varying thicknesses.

(4) A layer of 10 nm gold (Au) is deposited onto the wafer through electron beam evaporation (Denton e-beam evaporator) at $1 \times 10^{-6}$ Torr to protect the PDMS from swelling by organic solvent in subsequent steps.

(5) The procedure in step (2) is performed iteratively to sequentially coat an additional layer of SU-8.

Following the manufacturing process, the wafer is sectioned into samples measuring 10 mm × 5 mm, to be reserved for later use. The aforementioned thermal treatments entail an elevation in temperature from room temperature to the specified set temperature, followed by a 1-hour dwelling period at the set temperature, and ultimately a gradual reduction in temperature to return to room temperature.

For the PDMS thickness test shown in Fig. 2D and E, PDMS (10: 1) is spin coated at different speeds or mixed with hexane in various ratios and then spin coated at a constant speed of 6000 rpm.

### *2.1.2. Microwrinkle formation*

A VHB substrate with an aspect ratio of 5:1 with an initial length $L$ is first affixed onto a stretcher and stretched to a length of $L + \Delta L$. It is observed that the resultant wavelength is insensitive to $\Delta L/L$, provided it exceeds the critical strain, in agreement with classical wrinkle theories (Huang et al., 2005; Groenewold, 2001). Subsequently, the specimen prepared in Section 2.1.1 is immersed in deionized water for a duration of 20 min. The dextran layer will dissolve in D.I. water so that the SU-8/PDMS/Au/SU-8 laminated film will be released from the substrate. The detached free-standing multi-layer film is then picked up by cleaned glass slide and transferred onto the center of the pre-strained VHB tape (Fig. 2B(i)). Subsequently, the VHB tape is disengaged from the stretcher, releasing the strain in the substrate and inducing the formation of microwrinkles (Fig. 2B(ii)).

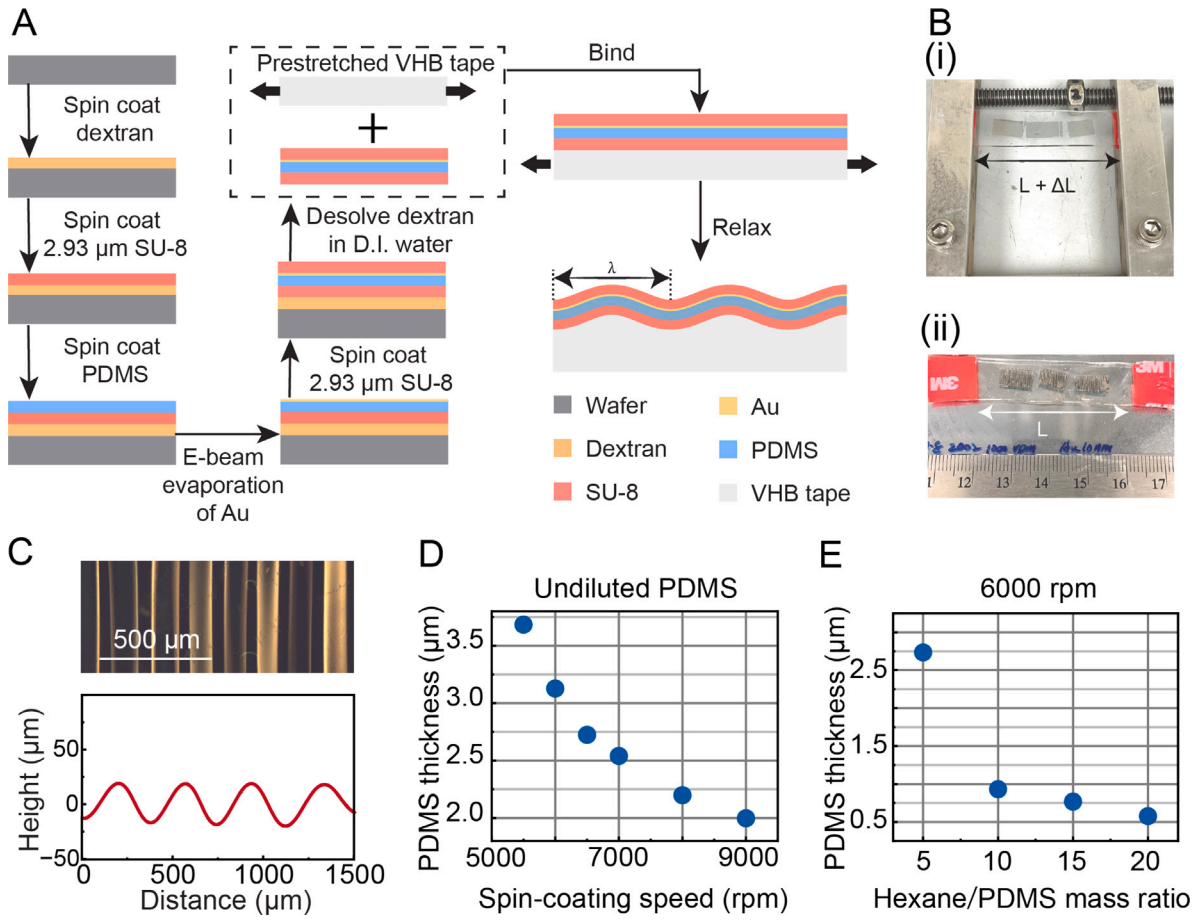


**Fig. 2.** (A) Schematic illustration of the fabrication and wrinkling procedures of the multilayer laminated beam. (B) The multilayer beam on VHB tape is (i) flat when the VHB tape is stretched and (ii) wrinkled when the stretch in the VHB tape is released. (C) A representative optical micrograph and the height profile of a wrinkled laminated beam. PDMS thickness as a function of (D) spin-coating speed for undiluted PDMS and (E) hexane/PDMS mass ratio at a spin-coating speed of 6000 rpm.

#### 2.1.3. Characterization

The thickness of PDMS and the microwrinkle profiles (Fig. 2C) are characterized by a DektakXT contact profilometer with 1–3 mg stylus force. The optical images are taken by an Olympus BX51M optical microscope.

### 2.2. Analytical model

In this work, we consider a laminated beam with $N+1$ stiff layers and $N$ soft layers stacked alternatively (Fig. 3A(i)). The $i$th layer has a Young's modulus of $E_i$, a Poisson's ratio of $\nu_i$, and a height of $h_i$. The beam is bounded to a semi-infinite incompressible substrate with modulus $E_s$. Specifically, the contribution of the gold layer to the mechanical behavior of the laminated film in experiment is negligible, as it is three orders of magnitude thinner than the adjacent SU-8 layer but only one order of magnitude stiffer. Therefore, the SU-8/PDMS/Au/SU-8 structure is effectively treated as a trilayer system of SU-8/PDMS/SU-8 in this work, representing the simplest configuration of laminated films. When subjected to compression, the film wrinkles into a sinusoidal shape with wavelength $\lambda$ and amplitude $A$ (Fig. 3A(ii)). In this section, we first follow the framework by Groenewold (Groenewold, 2001) to develop a general framework to determine the wavelength and critical strain of the wrinkling using an energy approach. We then discuss various beam theories and their solution for the wrinkling problem.

#### 2.2.1. General framework for wrinkling

The deflection of the wrinkled beam is characterized by a sinusoidal function as:

$$w = A\cos(kx), \tag{1}$$

where $w$ is the displacement in $y$ direction, $A$ is the amplitude of the wrinkle, $k = 2\pi/\lambda$ is the wave number. In this work, we assume small deflection, i.e., $A \ll \lambda$ and that the average membrane strain in the beam is zero (Groenewold, 2001). As a result, the

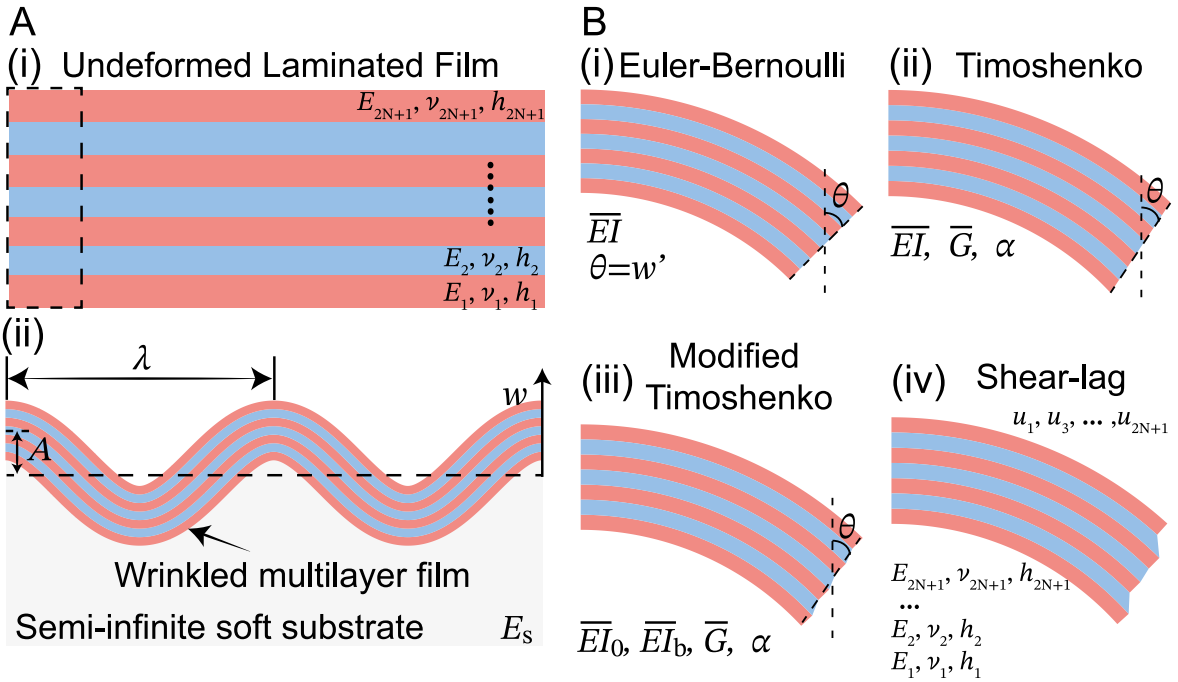


**Fig. 3.** (A) Schematic of a multilayer laminated film with extreme modulus mismatch, where red represents the stiff layers and blue represents the soft layers. The $i$th layer has a Young's modulus of $E_i$, a Poisson's ratio of $\nu_i$, and a height of $h_i$. (i) The undeformed, stress-free configuration. (ii) The wrinkled configuration with wavelength $\lambda$ and amplitude $A$ on a semi-infinite soft substrate. $w$ is the out-of-plane displacement (B) Deformed shapes of the black dash box in A(i), showing the cross-sections corresponding to different beam theories: (i) Euler–Bernoulli beam theory (EBT), (ii) Timoshenko beam theory (TBT), (iii) modified Timoshenko beam theory (MTBT), and (iv) Shear-lag theory.

amplitude $A$ can be written as a function of compressive strain of the beam before wrinkle $\epsilon_0$ and the wavelength $\lambda$:

$$A = \frac{2\sqrt{\epsilon_0}}{k}. \tag{2}$$

The curvature of the wrinkled beam $\kappa$ under small deflection is:

$$\kappa = w'' = -k^2 A\cos(kx) = -2\sqrt{\epsilon_0}k\cos(kx). \tag{3}$$

The elastic energy of the semi-infinite incompressible substrate due to wrinkling is:

$$U_{\text{sub}} = \frac{1}{6}E_s k A^2 = \frac{2E_s\epsilon_0}{3k}. \tag{4}$$

Let $U_{\text{beam}}^{\text{wrinkle}}(\epsilon_0, k)$ denote the elastic energy of the wrinkled beam per unit length. Its specific form depends on the beam theory adopted and will be discussed in the following sections. The total energy of the system is:

$$U_{\text{tot}} = U_{\text{sub}} + U_{\text{beam}}^{\text{wrinkle}}. \tag{5}$$

The wave number $k$ is determined by minimizing $U_{\text{tot}}$, which is determined by the following implicit equation:

$$\frac{\partial U_{\text{tot}}(k,\epsilon_0)}{\partial k} = -\frac{2E_s\epsilon_0}{3k^2} + \frac{\partial U_{\text{beam}}^{\text{wrinkle}}}{\partial k} = 0. \tag{6}$$

To solve for the critical compressive strain to induce wrinkle, we compare the total energy of the wrinkled system to the compressive energy of the beam without wrinkling. Let $U_{\text{tot}}^{\min}(\epsilon_0)$ be the minimized total energy in Eq. (5) for a given $\epsilon_0$. The compressive energy of the beam without wrinkling is written as $U_{\text{cprs}}(\epsilon_0) = \frac{1}{2}\overline{EA}\epsilon_0^2$, where $\overline{EA} = \sum \overline{E}_i h_i$ is the axial stiffness of the beam under plane strain condition, and $\overline{E}_i = \frac{1}{1-\nu_i^2}E_i$ is the plane strain modulus of the layer $i$. The critical strain $\epsilon_c$ is determined implicitly through the following equation:

$$U_{\text{cprs}}(\epsilon_c) = U_{\text{tot}}^{\min}(\epsilon_c). \tag{7}$$

### 2.2.2. Wrinkling of Euler–Bernoulli beam

As shown in Fig. 3B(i), the classic Euler–Bernoulli beam theory is based on two kinematic assumptions: (1) the cross section of the beam remains planar after bending, and (2) the cross section of the beam remains perpendicular to the deformed axis of the

beam. In small deflection, the second assumption is equivalent to prescribing the rotation angle of the cross-section $\theta$ as:

$$\theta = w'. \tag{8}$$

The bending energy per unit area can be written as a function of curvature $\kappa$ and flexural rigidity $\overline{EI}$ as:

$$U_{\text{beam}}^{\text{wrinkle}} = \frac{1}{\lambda}\int_0^{\lambda} \frac{1}{2}\overline{EI}\kappa^2 dx = \epsilon_0 \overline{EI} k^2. \tag{9}$$

$\overline{EI} = \sum_{i=1}^{i=2N+1} \overline{EI}_{\text{i}} + \sum_{i=1}^{i=2N+1} \overline{EA}_{\text{i}} y_{\text{i}}^2$ is a function of elastic modulus and thickness of each layer, where $\overline{EI}_{\text{i}} = \frac{1}{12}\frac{E_{\text{i}}}{1-\nu_{\text{i}}^2} h_{\text{i}}^3$, $\overline{EA}_{\text{i}} = \frac{E_{\text{i}}}{1-\nu_{\text{i}}^2} h_{\text{i}}$, and $y_i$ is the $y$ coordinate of the $i$th layer.

Substituting Eq. (9) into Eqs. (6) and (7), we can solve for the equilibrium wavelength $\lambda^{\text{EB}}$ and the critical compressive strain $\epsilon_{\text{c}}^{\text{EB}}$ for Euler–Bernoulli beams:

$$\lambda^{\text{EB}} = 2\pi \left(\frac{3\overline{EI}}{E_s}\right)^{1/3} \tag{10}$$

$$\epsilon_{\text{c}}^{\text{EB}} = \frac{(3\overline{EI})^{1/3} E_s^{2/3}}{\overline{EA}} \tag{11}$$

Specifically, for a homogeneous beam where $E_1 = E_2 = \cdots = E_{2N+1}$, $\nu_1 = \nu_2 = \cdots = \nu_{2N+1}$, we have $\overline{EI} = \frac{1}{12}\frac{E_1}{1-\nu_1^2} h^3$, $\overline{EA} = \frac{1}{1-\nu_1^2} E_1 h$, where $h = \sum_{i=1}^{2N+1} h_i$ is the total thickness of the beam, and the above equation reduces to the classical wrinkle theory:

$$\lambda = 2\pi h \left(\frac{\overline{E}_1}{4E_s}\right)^{1/3} \tag{12}$$

$$\epsilon_{\text{c}} = \frac{1}{4}\left(\frac{4E_s}{\overline{E}_1}\right)^{2/3} \tag{13}$$

### 2.2.3. Wrinkling of Timoshenko beam

Timoshenko beam theory (TBT) is widely used for short beams or beams under dynamic loading. It retains the first kinematic assumption in Euler–Bernoulli beam theory but relaxes the constraint on the cross section rotation by considering the shear deformation in the beam (Fig. 3B(ii)). When the deflection $w$ is given, the rotation angle $\theta$ can be solved through the following equation:

$$\frac{\mathrm{d}w}{\mathrm{d}x} = \theta - \frac{\overline{EI}}{\alpha \overline{G} h}\frac{\mathrm{d}^2\theta}{\mathrm{d}x^2} \tag{14}$$

where $h$ is the total thickness of the beam, $\overline{G}$ is the effective shear modulus of the laminated beam, and $\alpha$ is the geometry dependent Timoshenko shear coefficient. The values of $\overline{G}$ and $\alpha$ for laminated composite can be found in the work by Qin et al. (2020). Plugging in Eq. (1), we can solve the rotation angle $\theta$ to be:

$$\theta = -\frac{2\sqrt{\epsilon_0}}{1+\beta^{\text{TBT}}k^2}\sin kx, \quad \beta^{\text{TBT}} = \frac{\overline{EI}}{\alpha \overline{G} h} \tag{15}$$

The elastic energy of beam per unit area is calculated as:

$$\begin{aligned} U_{\text{beam}}^{\text{wrinkle}} &= \frac{1}{\lambda}\int_0^{\lambda}\left[\frac{1}{2}\overline{EI}\left(\frac{\mathrm{d}\theta}{\mathrm{d}x}\right)^2 + \frac{\alpha\overline{G}h}{2}\left(\theta - \frac{\mathrm{d}w}{\mathrm{d}x}\right)^2\right] dx \\ &= \epsilon_0 \overline{EI}\frac{k^2}{1+\beta^{\text{TBT}}k^2} \end{aligned} \tag{16}$$

The wave number and the critical strain can be solved numerically by plugging Eq. (16) into Eqs. (6), (7).

### 2.2.4. Wrinkling of modified Timoshenko beam

Qin et al. (2020) proposed a modified Timoshenko beam theory (MTBT) for multilayer 2D materials and laminated materials, where the Timoshenko beam theory tends to overestimate the flexural rigidity and can predict unphysical deformation under certain loading conditions. In this section, we give a brief recaption of MTBT and apply it to the wrinkle problem. MTBT maintains the kinematic assumption of TBT in an average sense and also uses the rotation of the cross section $\theta$ and the deflection $w$ to describe the deformation of the beam (Fig. 3B(iii)). Locally, it assumes that each stiff layer still follows the Euler–Bernoulli beam theory, which is equivalent to assuming a zigzag cross-sectional shape after deformation. In MTBT, the flexural rigidity is split into two parts $\overline{EI}_0$ and $\overline{EI}_{\text{b}}$:

$$\overline{EI}_{\text{b}} = \sum_{i=1}^{i=2N+1} \overline{EI}_{\text{i}}, \quad \overline{EI}_0 = \overline{EI} - \overline{EI}_{\text{b}}, \tag{17}$$

where $\overline{EI}_0$ is the sum of flexural rigidity of stiff layers, and $\overline{EI}_\mathrm{b}$ is the remainder of total flexural rigidity predicted by Euler–Bernoulli beam theory. The governing equation for $\theta$ is:

$$\frac{\mathrm{d}w}{\mathrm{d}x} = \theta - \frac{\overline{EI}_0}{\alpha\overline{G}h}\frac{\mathrm{d}^2\theta}{\mathrm{d}x^2}, \tag{18}$$

where $\overline{G}$ and $\alpha$ are the same effective shear modulus of laminated beam and the Timoshenko shear coefficient as in Timoshenko beam theory. Plugging in Eq. (1), we can solve the rotation angle to be:

$$\theta = -\frac{2\sqrt{\epsilon_0}}{1+\beta^{\mathrm{MTBT}}k^2}\sin kx, \quad \beta^{\mathrm{MTBT}} = \frac{\overline{EI}_0}{\alpha\overline{G}h}. \tag{19}$$

The elastic energy of the film per unit area is

$$\begin{aligned} U_{\mathrm{bend}} &= \frac{1}{\lambda}\int_0^\lambda \left[\frac{1}{2}\overline{EI}_b\left(\frac{\mathrm{d}^2w}{\mathrm{d}x^2}\right)^2 + \frac{1}{2}\overline{EI}_0\left(\frac{\mathrm{d}\theta}{\mathrm{d}x}\right)^2 + \frac{\alpha\overline{G}h}{2}\left(\theta - \frac{\mathrm{d}w}{\mathrm{d}x}\right)^2\right]dx \\ &= \epsilon_0\left[\overline{EI}_\mathrm{b}k^2 + \overline{EI}_0\frac{k^2}{1+\beta^{\mathrm{MTBT}}k^2}\right] \end{aligned} \tag{20}$$

The wave number and the critical strain can be solved numerically by plugging Eq. (20) into Eqs. (6), (7).

### 2.2.5. *Wrinkling of beam with shear-lag*

In shear-lag theory, both kinematic assumptions in Euler–Bernoulli beam theory are dropped and the cross section can deform into any zig-zag shape that minimizes the elastic energy (Fig. 3B(iv)). The deformation must be described by deflection $w$ and axial displacement in each stiff layer $u_{2k-1}$. The membrane strain in each stiff layer is $\epsilon_{2k-1} = \frac{\mathrm{d}u_{2k-1}}{\mathrm{d}x}$. Our previous work established the relationship between the shear strain in the soft layers $\gamma_{2k}$ and the axial displacements in the stiff layers for large deflection. In this work, we use a linearized form:

$$\gamma_{2k} = \frac{1}{h_{2k}}\left[u_{2k-1} - u_{2k+1} + (h_{2k} + h_{2k-1}/2 + h_{2k+1}/2)\frac{\mathrm{d}w}{\mathrm{d}x}\right] \tag{21}$$

The total elastic energy in the beam can be written as:

$$U_{\mathrm{beam}} = \underbrace{\sum_{k=1}^{N+1}\frac{1}{\lambda}\int_0^\lambda \frac{1}{2}\overline{EI}_{2k-1}\kappa^2 dx}_{U_{\mathrm{beam}}^{\mathrm{bend}}} + \underbrace{\sum_{k=1}^{N+1}\frac{1}{\lambda}\int_0^\lambda \frac{1}{2}\overline{EA}_{2k-1}\epsilon_{2k-1}^2 dx}_{U_{\mathrm{beam}}^{\mathrm{stretch}}} + \underbrace{\sum_{k=1}^{N}\frac{1}{\lambda}\int_0^\lambda \frac{1}{2}G_{2k}h_{2k}\gamma_{2k}^2 dx}_{U_{\mathrm{beam}}^{\mathrm{shear}}} \tag{22}$$

where $U_{\mathrm{beam}}^{\mathrm{bend}}$ represents the bending energy in the stiff layers, $U_{\mathrm{beam}}^{\mathrm{stretch}}$ represents the stretching energy in the stiff layers, and $U_{\mathrm{beam}}^{\mathrm{shear}}$ represents the shear energy in the soft layers. The stretching energy and bending energy in the soft layers are neglected due to the extreme modulus mismatch. For a more general case where the stiff and soft layers do not stack alternatively, the adjacent stiff layers can be considered a single stiff layer described by the composite Euler–Bernoulli beam, while additional kinematic assumption and energy analysis needs to be made to derive an equivalent shear modulus for adjacent soft layers. The governing equation and the boundary condition for $u_{2k-1}$ is obtained by taking variation of $U_{\mathrm{beam}}$ with respect to $u_{2k-1}$ and implementing linearization and normalization:

$$\frac{\mathrm{d}^2\mathbf{u}}{\mathrm{d}\hat{x}^2} = \Pi^2\left[\hat{\mathbf{C}}\hat{\mathbf{A}}\mathbf{u} - \hat{\mathbf{C}}\hat{\mathbf{b}}\frac{\mathrm{d}w}{\mathrm{d}\hat{x}}\right] \tag{23}$$

$$\mathbf{u}|_{\hat{x}=0} = \mathbf{u}|_{\hat{x}=1}, \quad \left.\frac{\mathrm{d}\mathbf{u}}{\mathrm{d}\hat{x}}\right|_{\hat{x}=0} = \left.\frac{\mathrm{d}\mathbf{u}}{\mathrm{d}\hat{x}}\right|_{\hat{x}=1} \tag{24}$$

where $\mathbf{u} = [u_1, u_3, \ldots, u_{2N+1}]^T$, $\hat{x} = x/\lambda$ is the normalized coordinate, $\Pi = \sqrt{(1-\nu_1^2)\frac{G_2}{E_1}\frac{\lambda^2}{h_1h_2}}$ is the dimensionless shear-lag number,

$$\hat{\mathbf{C}} = \begin{bmatrix} 1 & & & & & \\ & \frac{\overline{EA}_1}{\overline{EA}_3} & & & & \\ & & \frac{\overline{EA}_1}{\overline{EA}_5} & & & \\ & & & \ddots & & \\ & & & & \frac{\overline{EA}_1}{\overline{EA}_{2N+1}} & \end{bmatrix},$$

$$\hat{\mathbf{A}} = \begin{bmatrix} 1 & -1 & & & & \\ -1 & 1+\frac{G_4}{h_4}\frac{h_2}{G_2} & -\frac{G_4}{h_4}\frac{h_2}{G_2} & & & \\ & -\frac{G_4}{h_4}\frac{h_2}{G_2} & \ddots & \ddots & & \\ & & \ddots & \ddots & -\frac{G_{2N}}{h_{2N}}\frac{h_2}{G_2} & \\ & & & -\frac{G_{2N}}{h_{2N}}\frac{h_2}{G_2} & \frac{G_{2N}}{h_{2N}}\frac{h_2}{G_2} & \end{bmatrix},$$

$$\hat{\mathbf{b}} = \begin{bmatrix} \frac{0.5h_1+0.5h_3+h_2}{h_1+h_2} \\ \frac{G_4}{h_4}\frac{h_2}{G_2}\frac{0.5h_3+0.5h_5+h_4}{h_1+h_2} - \frac{0.5h_1+0.5h_3+h_2}{h_1+h_2} \\ \frac{G_6}{h_6}\frac{h_2}{G_2}\frac{0.5h_5+0.5h_7+h_6}{h_1+h_2} - \frac{G_4}{h_4}\frac{h_2}{G_2}\frac{0.5h_3+0.5h_5+h_4}{h_1+h_2} \\ \vdots \\ -\frac{G_{2N}}{h_{2N}}\frac{h_2}{G_2}\frac{0.5h_{2N-1}+0.5h_{2N+1}+h_{2N}}{h_1+h_2} \end{bmatrix}.$$

Plugging the Eq. (1) into Eq. (23), we can solve the axial displacements and the membrane strains in the stiff layers:

$$\mathbf{u} = -2\sqrt{\epsilon_0}\sin(2\pi\hat{x})\sum_{i=2}^{i=N+1}\frac{g_i\Pi^2}{k^2+\Pi^2\hat{\lambda}_i}\hat{\mathbf{v}}_i, \tag{25}$$

where $\hat{\lambda}_i$ is the eigenvalues of $\hat{\mathbf{C}}\hat{\mathbf{A}}$ in ascending order, $\hat{v}_i$ is the corresponding eigenvalues, and $\hat{\mathbf{C}}\hat{\mathbf{b}} = \sum_{i=1}^{i=N+1} g_i\hat{\mathbf{v}}_i$. It can be shown that the solution reduces to the Euler–Bernoulli beam theory when $\Pi$ approaches infinity (Wang et al., 2024a).

The wavelength can be determined by combining Eqs. (6), (7), (22), (25). Inspired by Eq. (10), we define the equivalent flexural rigidity in a consistent manner with the wrinkling of Euler–Bernoulli beams:

$$D = \frac{E_s}{3}\left(\frac{\lambda}{2\pi}\right)^3. \tag{26}$$

It can be shown the equivalent flexural rigidity defined in Eq. (26) is equivalent to the intrinsic definition of flexural rigidity in an energy perspective Appendix B.

#### 2.2.6. Frictionless interface model

In this section we consider a special case of the shear-lag model where $\Pi$ approaches zero. In this limit, Eq. (25) reduces to $\mathbf{u} = 0$, indicating that the axial displacements and membrane strains in all the stiff layers are zero. Physically, this scenario suggests that the stiff layers can glide over each other freely, akin to a frictionless interface. Thus, we refer to this case as the frictionless interface model. Specifically, when all stiff layers possess identical elastic properties $E_1$, $\nu_1$ and height $h_1$ and all soft layers also have identical shear modulus $G_2$ and height $h_2$, the frictionless interface model predicts the wrinkle wavelength, equivalent flexural rigidity, and the critical strain to induce wrinkle to be:

$$\lambda^{\mathrm{FI}} = 2\pi\left(\frac{3(N+1)\overline{EI}_1}{E_s}\right)^{1/3} \tag{27}$$

$$D^{\mathrm{FI}} = (N+1)\overline{EI}_1 \tag{28}$$

$$\epsilon_c^{\mathrm{FI}} = (N+1)^{-2/3}\frac{(3\overline{EI}_1)^{1/3}E_s^{2/3}}{\overline{EA}_1} \tag{29}$$

### 2.3. Finite element model

An ABAQUS finite element model (FEM) is developed to validate our theory (Fig. 4). The FEM consists of a laminated film of length $L$ placed on a soft substrate with thickness $h_{\mathrm{sub}}$. The left and right ends of the model are fixed in the $x$-direction, while the bottom surface of the substrate is fixed in both x- and $y$-directions. Following the approach of Chen and Hutchinson (2004), wrinkling is induced in the laminated film via artificial thermal expansion. An artificial coefficient of thermal expansion (CTE) of $\alpha = 0.05$ is used for the multilayer film, with a CTE of zero for the substrate. The temperature field was assigned to increase from 0 to 1 during the simulation. Due to the constraints imposed by the boundary conditions, the number of wrinkles is restricted to integer or half-integer values. To minimize the wavelength error in the simulations to within ±5%, the model length L is chosen to be at least ten times the wavelength of the wrinkle. The thickness of the substrate $h_{\mathrm{sub}}$ is selected to be greater than the wavelength of the wrinkle to ensure that the finite thickness effect of the substrate is negligible (Huang et al., 2005).

The model is discretized using a structured mesh with CPE4R elements. The stiff and soft layers of the laminated film are meshed uniformly, while a biased mesh is applied to the substrate to increase mesh density near the film–substrate interface. A Poisson's ratio of 0.48 is assigned to the soft layers to approximate incompressibility. A linear buckling analysis is first performed to obtain the eigenmodes, and the first eigenmode is scaled and imposed as a geometric imperfection. The maximum amplitude of the introduced imperfection is set at 2% of the total thickness of the laminated film. The wavelength of the wrinkle in the simulation consistently followed the introduced imperfection.

## 3. Results

For simplification, we focus on the case where $E_1 = E_3 = \ldots = E_{2N+1}$, $\nu_1 = \nu_3 = \ldots = \nu_{2N+1}$, $h_1 = h_3 = \ldots = h_{2N+1}$, $G_2 = G_4 = \ldots = G_{2N}$, $h_2 = h_4 = \ldots = h_{2N}$. The baseline geometric parameters and material properties are chosen to be $h_1 = 2.93\,\mu\mathrm{m}$, $h_2 = 1.00\,\mu\mathrm{m}$, $N = 1$, $E_1 = 2.0$ GPa, $\nu_1 = 0.22$, $E_2 = 2$ MPa, $\nu_2 = 0.5$, and $E_{\mathrm{sub}} = 175\,\mu\mathrm{m}$ based on our experimental system.

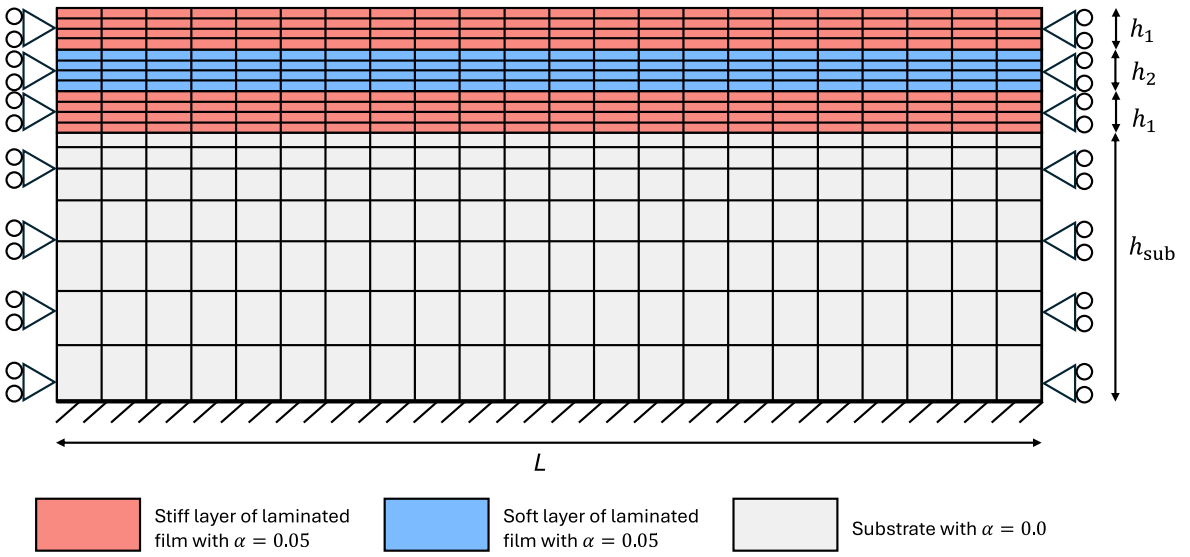


**Fig. 4.** Schematic for finite element model of laminated film wrinkling on soft substrate. The wrinkle is induced by artificial thermal expansion in the model.

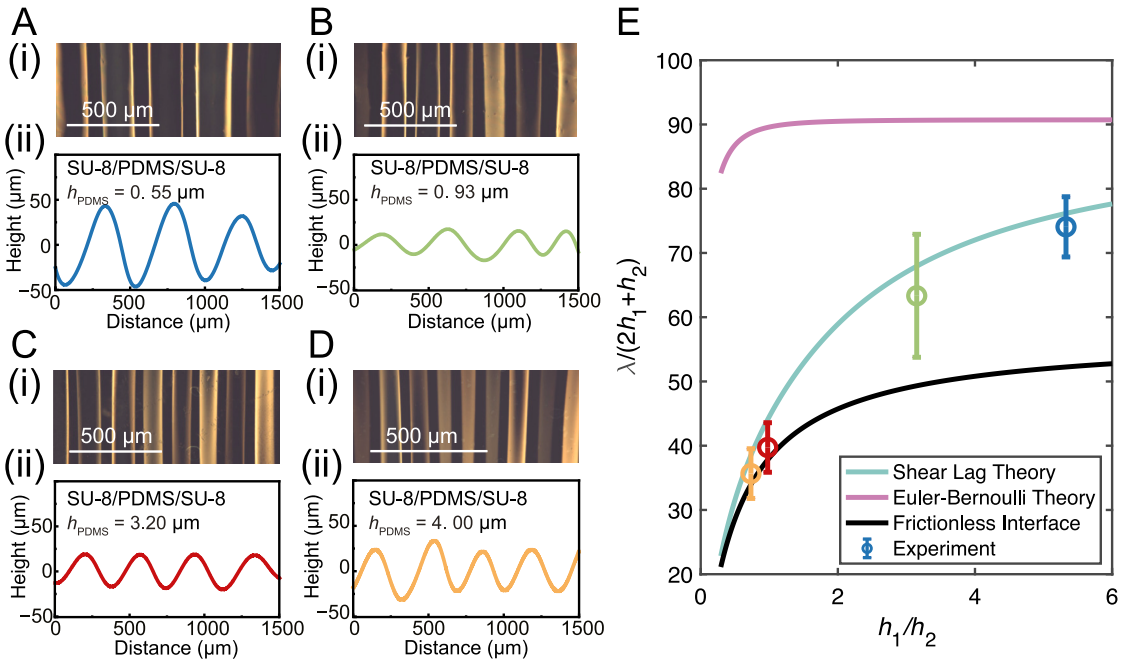


**Fig. 5.** Optical micrographs and corresponding height profiles of wrinkles in SU-8/PDMS/SU-8 trilayer films with SU-8 thickness of 2.93 μm and varying PDMS thicknesses: (A) 0.55 μm, (B) 0.93 μm, (C)3.20 μm, and (D) 4.00 μm. (E) Normalized wrinkle wavelength as a function of the stiff-to-soft layer thickness ratio, comparing predictions from shear-lag theory (teal curve), Euler–Bernoulli beam theory (purple curve), and the frictionless interface model (black curve) with experimental measurements (markers with error bars). The shear-lag theory is in good agreement with experimental results. The colors of the markers are consistent with the curve colors in A-D.

### 3.1. *Effect of layer thickness ratio*

Fig. 5A-D present optical micrographs and wrinkle profiles of the laminated films with varying PDMS thicknesses, ranging from 0.55 μm to 4.00 μm. The parameters are chosen to span a wide range, from those close to frictionless interface to those approximating the Euler–Bernoulli beam theory. Due to fabrication limitations, the minimum achievable PDMS thicknesses is 550 nm. The experimentally measured normalized wrinkle wavelength is plotted against the stiff-to-soft layer thickness ratio $h_1/h_2$, and compared to predictions from the shear-lag theory, the Euler–Bernoulli beam theory, and the frictionless interface model (Fig.

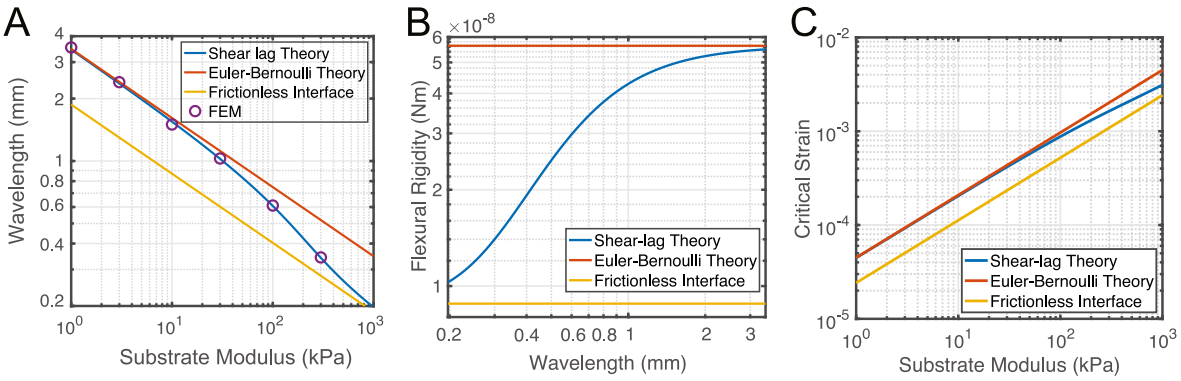


**Fig. 6.** (A) The wrinkle wavelength of the laminated beam with shear-lag (blue curve) decreases with increasing substrate modulus, showing good agreement with the FEM results (purple dots). (B) The equivalent flexural rigidity of the laminated beam increases with wrinkle wavelength. (C) Critical strain to wrinkle increases with increasing substrate modulus. All three parameters approach Euler–Bernoulli beam theory (red line) at low substrate modulus or large wavelength and the frictionless interface model (yellow line) at high substrate modulus or small wavelength.

5E). All three theories predict an increase in normalized wavelength as the stiff-to-soft layer thickness ratio increases, attributed to the enhanced stiffness of the laminated beam, which is positively correlated with the wrinkle wavelength. As expected, the shear-lag theory predicts a wavelength higher than the frictionless interface model but lower than that of the Euler–Bernoulli beam theory, a trend observed in all subsequent parameter studies. As $h_1/h_2$ increases, the shear-lag number $\Pi$ increases, leading the shear-lag theory results to transition from the frictionless interface model towards the Euler–Bernoulli theory. The shear-lag theory demonstrates reasonable agreement with the experimental results in all thickness ratios tested, while the Euler–Bernoulli theory and the frictionless interface model show significant deviations, particularly at higher $h_1/h_2$ values.

### 3.2. *Effect of substrate modulus*

Fig. 6A plots the wrinkle wavelength as a function of the substrate modulus for the shear-lag theory, the Euler–Bernoulli theory and the frictionless interface model. Both the Euler–Bernoulli beam theory and the frictionless interface predict a relationship of $\lambda \propto E_s^{-1/3}$, which appears as straight lines with a slope of $-1/3$ in a log–log plot. This power-law behavior with an exponent of $-1/3$ aligns with the classic wrinkling theory for homogeneous beams (Eq. (12)). Although shear-lag theory also predicts a reduction in wrinkle wavelength with increasing substrate modulus, the relationship is not a simple power law. At lower substrate modulus, the predictions of the shear-lag theory closely match those of the Euler–Bernoulli theory. However, as the substrate modulus increases, the wrinkle wavelength and the shear-lag number both decrease, leading the shear-lag theory to approach the frictionless interface prediction. The FEM results show good agreement with the predictions of the proposed shear-lag theory across all cases considered, with an error always below 3%, as will be further demonstrated in the following sections. The minor discrepancy is mainly attributed to the constraint that the number of wrinkle waves must be integer or half-integer values in the numerical simulation. For cases where the relative error exceeds 1%, it is confirmed that the wavelength predicted by the shear-lag theory consistently falls between the wavelengths of the first and second eigenmodes obtained from the linear buckling analysis.

Fig. 6B plots the equivalent flexural rigidity of the laminated beam for varying the substrate modulus as a function of the wavelength of the wrinkle. The equivalent flexural rigidity increases in the following order: frictionless interface, shear-lag theory, and Euler–Bernoulli theory. This trend is consistent with our previous findings on the bending of laminated beams (Wang et al., 2024a) and is observed throughout all subsequent parameter studies. Both the frictionless interface and the Euler–Bernoulli theory predict a constant flexural rigidity, independent of the substrate modulus and wrinkle wavelength. In contrast, shear-lag theory shows an increase in equivalent flexural rigidity with increasing wavelength, reflecting the distinct length dependence that has previously been reported (Li et al., 2016). This phenomenon is attributed to the increase in shear-lag number $\Pi$ with increasing wavelength. At smaller wavelengths, $\Pi$ is small, and shear-lag theory approaches frictionless interface model. At larger wavelengths, $\Pi$ becomes large, and the shear-lag theory approaches the predictions of the Euler–Bernoulli beam theory.

Fig. 6C plots the critical strain of the laminated beam as a function of the substrate modulus on a log–log scale. All three theories predict an increase in critical strain with increasing substrate modulus. Both the Euler–Bernoulli theory and the frictionless interface model predict $\epsilon_c \propto E_s^{2/3}$, consistent with the classic wrinkling theory (Eq. (13)). Although classic theory suggests that a more compliant beam leads to a higher critical strain, the comparison among the three models reveals the opposite trend: the stiffest beam, as described by Euler–Bernoulli theory, exhibits the highest critical strain, while the softest, represented by the frictionless interface, shows the lowest critical strain. This contrast underscores that a multilayer beam with shear-lag effects cannot be treated simply as a homogeneous beam with a lower effective Young's modulus. Similarly to the trends observed for wavelength and equivalent flexural rigidity, the predicted critical strain follows a nonpower-law relationship, approaching the Euler–Bernoulli theory at low substrate modulus and the frictionless interface behavior at high substrate modulus.

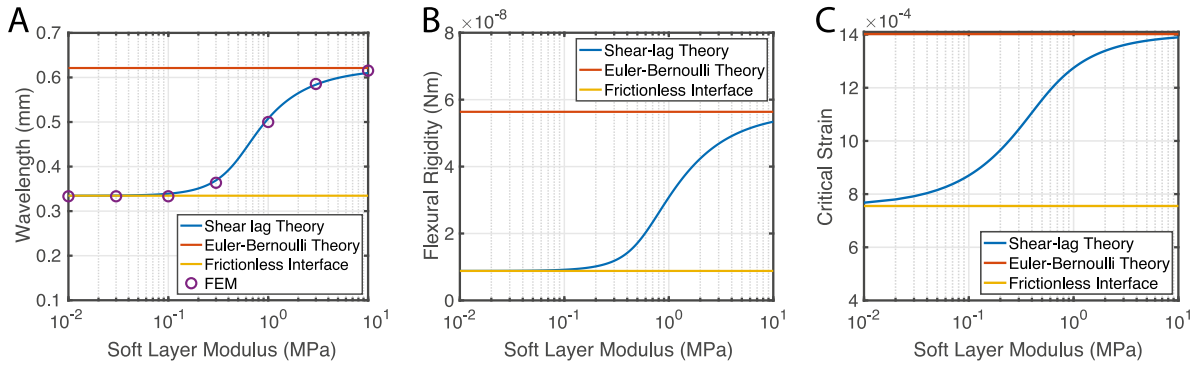


**Fig. 7.** (A) The wrinkle wavelength, (B) equivalent flexural rigidity, and (C) critical strain of the laminated beam with shear-lag all increase with the soft layer modulus, approaching the Euler–Bernoulli beam theory at high modulus and the frictionless interface model at low modulus.

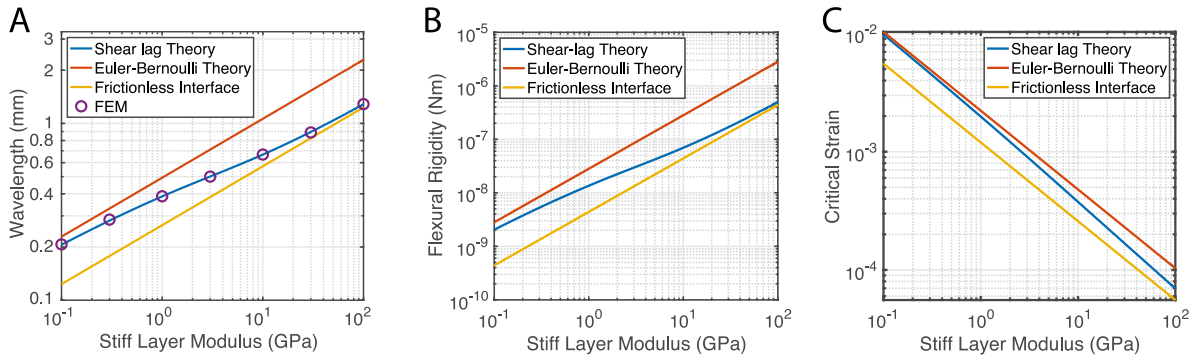


**Fig. 8.** (A) The wrinkle wavelength and (B) the flexural rigidity of the laminated beam with shear-lag increase with increasing stiff layer modulus whereas (C) the critical strain to wrinkling decreases with increasing stiff layer modulus, all converging to Euler–Bernoulli theory at low stiff layer modulus and to the frictionless interface model at high stiff layer modulus.

### 3.3. Effect of soft layer modulus

Fig. 7 A–C present the wrinkle wavelength, the equivalent flexural rigidity, and the critical strain as functions of the soft layer modulus in the laminated beam for the shear-lag theory, the Euler–Bernoulli theory, and the frictionless interface model. As anticipated, the frictionless interface model predicts that the wavelength, flexural rigidity, and critical strain are independent of the soft layer modulus, as the contribution of the soft layer to the total elastic energy is neglected. Similarly, the Euler–Bernoulli theory predicts that these parameters are nearly independent of the soft layer modulus. This occurs because the contribution of the soft layer modulus $G_2$ to the flexural rigidity $\overline{EI}$ is minimal, given that $E_1 \gg G_2$. For all three parameters investigated, including wavelength, flexural rigidity, and critical strain, the predictions from the shear-lag theory increase from values close to those predicted by the frictionless interface at low soft layer modulus and approach those predicted by the Euler–Bernoulli theory at higher soft layer modulus. This behavior is driven by the increase in the shear-lag number $\Pi$ with increasing soft layer modulus.

### 3.4. Effect of stiff layer modulus

Fig. 8A–C plot the wrinkle wavelength, the equivalent flexural rigidity, and the critical strain as functions of the stiff layer modulus $E_1$ in laminated beams for the shear-lag theory, the Euler–Bernoulli theory, and the frictionless interface model. The frictionless interface theory predicts that $\lambda \propto E_1^{1/3}$, $D \propto E_1$, and $\epsilon_c \propto E_1^{-2/3}$, which aligns with the classic wrinkle theory for homogeneous beams. A similar trend is observed for the Euler–Bernoulli theory, as the flexural properties of laminated beams are dominated by the properties of the stiff layer. The shear-lag theory predicts values that lie between those of the Euler–Bernoulli theory and the frictionless interface. The behavior of the shear-lag number $\Pi$ is controlled by two competing factors: the increasing stiff layer modulus, which tends to decrease $\Pi$, and the increasing wavelength, which tends to increase $\Pi$. In our combinations of parameters, the increase in the stiff layer modulus outraces the increase in wavelength. Therefore, the shear-lag number decrease with increasing stiff layer modulus, causing the shear-lag theory to approach the Euler–Bernoulli theory at low $E_1$ and the frictionless interface model at high $E_1$.

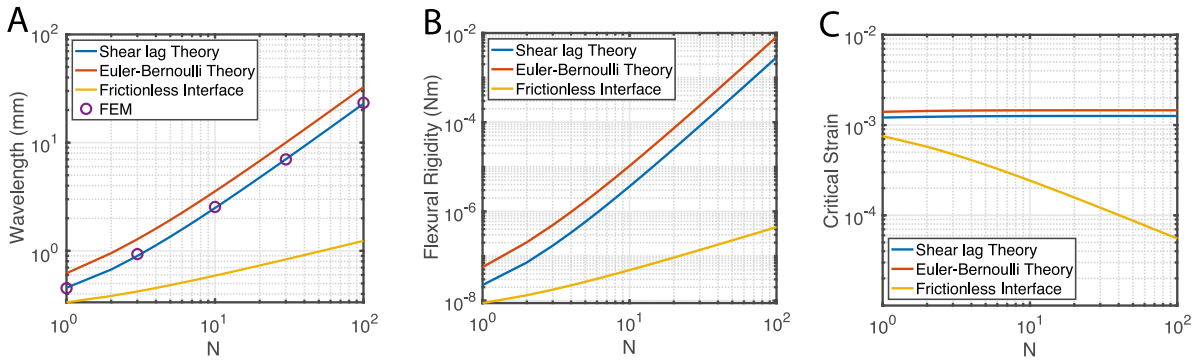


**Fig. 9.** (A) The wrinkle wavelength of the laminated beam and (B) the flexural rigidity of the laminated beam increase with the number of layers for all three models. (C) The critical strain remains constant at large layer numbers for Euler–Bernoulli beam theory and shear-lag theory, while it decreases with increasing number of layers for the frictionless interface model.

### *3.5. Effect of stiff layer number N+1*

Fig. 9A plots the wrinkle wavelength as a function of the soft layer number $N$ (ranging from 1 to 100) for the Euler–Bernoulli theory, shear-lag theory, and the frictionless interface model. On a log–log scale, all three models predict an increase in wavelength with increasing layer number, characterized by a smaller slope at low $N$ and a gradual approach to a straight line at large $N$. Both the Euler–Bernoulli and shear-lag theories predict $\lambda \propto N$ for large $N$, while the frictionless interface model predicts $\lambda \propto N^{1/3}$. Similarly, the Euler–Bernoulli and shear-lag theories predict that $D \propto N^3$, while the frictionless interface model predicts $D \propto N$ for large layer numbers (Fig. 9B). This distinct scaling behavior of flexural rigidity between the frictionless interface and Euler–Bernoulli theory has also been reported in our previous work (Wang et al., 2024a). As shown in Fig. 9C, both the Euler–Bernoulli and shear-lag theories predict a constant critical strain at large $N$, while the frictionless interface model predicts a decreasing critical strain, scaled as $N^{-2/3}$. Notably, the scaling law of the Euler–Bernoulli theory aligns with the conventional wrinkling theory for homogeneous beams, suggesting that laminated beams following the Euler–Bernoulli model can be approximated as homogenized composite beams when the number of layers is sufficiently large. Interestingly, while our previous work on fixed-size beams conforming to an arch showed that a larger layer number strengthens the shear-lag effect (Wang et al., 2024a), the wrinkle problem exhibits the opposite trend. This is because, in the wrinkle problem, the wavelength, which corresponds to the beam length in the previous study, also increases with the number of layers $N$.

## 4. Discussion

### *4.1. Energy contribution*

Fig. 10 shows the relative contributions of different energy components in the wrinkling of laminated beams with shear-lag. The components include membrane energy and bending energy within the stiff layers, shear energy within the soft layers, and substrate energy, all plotted against the wrinkle wavelength, which is varied by adjusting the substrate modulus while keeping other parameters constant. At small wavelengths, the shear-lag number $\Pi$ is small, causing the shear-lag theory to approach the frictionless interface model. Consequently, the membrane energy in the stiff layers approaches zero, as the membrane strain is zero in the frictionless interface model. Similarly, the shear energy in the soft layers also approaches zero because the frictionless interface model represents a soft layer with negligible modulus, resulting in minimal shear energy. As the wavelength increases, $\Pi$ increases, and the shear-lag theory converges towards the Euler–Bernoulli beam theory. This leads to a monotonic increase in the relative contributions of the membrane energy and a decrease in the contribution of the bending energy. The shear energy first increases and then decreases as the wavelength increases. At large wavelengths, the shear energy approaches zero again, consistent with the Euler–Bernoulli beam theory, where the shear strain is zero. Regardless of wavelength, the substrate energy is always twice the sum of the bending and membrane energies within the stiff layers, a relationship that can be mathematically proven for arbitrary layer properties and layer numbers Appendix A. This finding aligns with the classic wrinkle theory, where the energy of the substrate is twice the energy of the beam.

### *4.2. Comparison to TBT and MTBT*

Fig. 11A compares the predicted wrinkle wavelength from the shear-lag theory, Timoshenko beam theory (TBT) and the modified Timoshenko beam theory (MTBT) across the substrate modulus ranging from 1 kPa to 10 MPa. The prediction of MTBT closely aligns with the shear-lag theory, with a maximum relative error in wavelength of 13.5%, corresponding to a 46.5% error in the equivalent flexural rigidity. The TBT also shows good agreement with both the MTBT and shear-lag theory at low substrate modulus

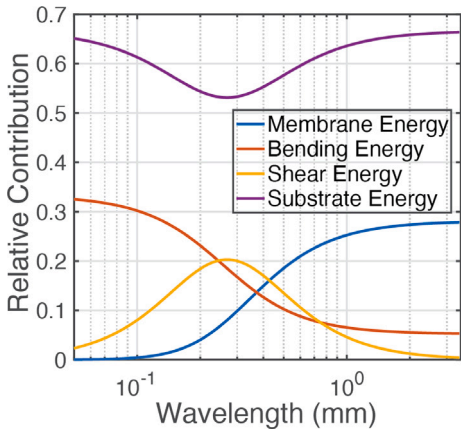


**Fig. 10.** The relative contributions of membrane energy in the stiff layers (blue curve), bending energy in the stiff layer (red curve), shear energy in the soft layers (yellow curve), and substrate energy (purple curve) to the total energy of the trilayer laminated beam wrinkling on semi-infinite substrate as functions of wrinkle wavelength. The wavelength is varied by adjusting the substrate modulus while keeping the beam properties fixed.

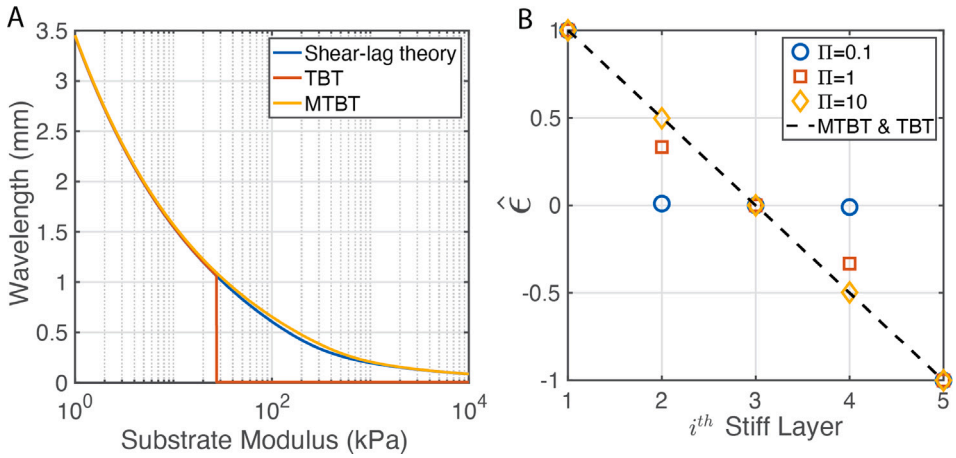


**Fig. 11.** (A) MTBT, TBT and Shear-lag theory predict similar wavelengths at small substrate modulus. However, the Timoshenko Beam Theory (TBT) predicts an unphysical jump at small wavelengths. (B) The shear-lag Theory predicts a linear distribution of membrane strain similar to MTBT and TBT at large shear-lag numbers ($\Pi$), but a nonlinear distribution at small $\Pi$.

(or large wavelengths), but it predicts an unphysical discontinuity, where the total energy minimizes at the 0 wavelength for higher substrate modulus. This abrupt change occurs because the Timoshenko beam theory overestimates the compliance of the laminated beam when the shear deformability is significant. Similar behavior can be observed when applying the Timoshenko beam theory to the three-point bending test of 2D materials (Qin et al., 2020). A similar behavior is observed in the comparison among shear-lag theory and MTBT across all other investigated parameters, as presented in the Supplementary Information.

Fig. 11B plots the normalized membrane strain in each stiff layer, normalized by the membrane strain in the first layer for shear-lag theory, modified Timoshenko beam theory (MTBT), and standard Timoshenko beam theory (TBT). As described in the Methods section, both the MTBT and the TBT assume that the cross section remains planar after deformation, leading to a linear distribution of membrane strain. The distribution of membrane strain in shear-lag theory depends on the shear-lag number $\Pi$. When $\Pi$ is large, the shear-lag theory converges towards the Euler–Bernoulli beam theory, resulting in an almost linear strain distribution across the layers. In contrast, when $\Pi$ is small, shear-lag effects become significant, leading to a nonlinear distribution of normalized membrane strain. This suggests that while the MTBT provides reasonable predictions for wavelength and equivalent flexural rigidity, its estimation of membrane strain may introduce significant errors, which are crucial for determining the bendability of the laminated structure. For an in-depth analysis of membrane strain profiles across layers and possible simplified solution, the readers are referred to the work by Shen et al. (2024).

### 4.3. Wrinkle test vs three point bending test

In a standard three-point bending test with small deflections, the beam's self-weight does not influence the bending stiffness, i.e., the slope of the force–deflection curve, due to the superposition principle in linear elasticity. However, when the deflection is

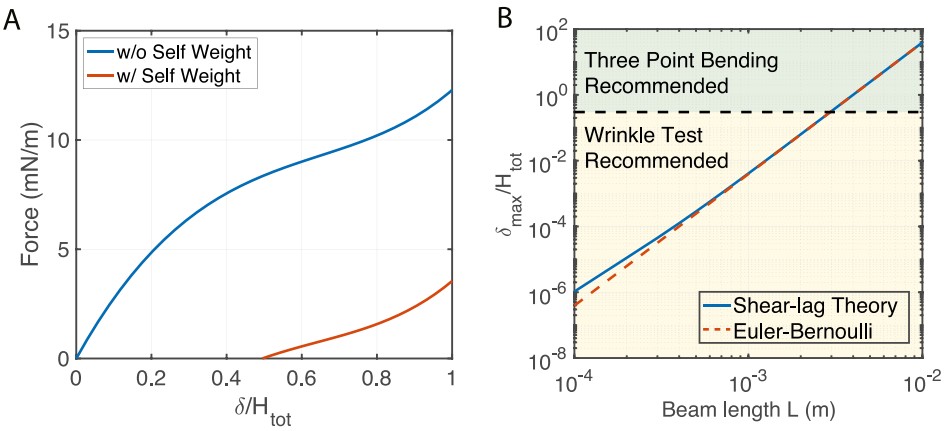


**Fig. 12.** (A) FEM simulation of deflection–force curve for three point bending test with and without self weight. (B) The normalized maximum deflection caused by self-weight increases with increasing beam length, causing significant geometrical nonlinearity at large beam length (black dash line).

comparable to film thickness, membrane stress can cause significant non-linearity, necessitating nonlinear theories such as Föppl–von Kármán theory or Kirchhoff–Love theory (Timoshenko and Woinowsky-Krieger, 1959). In these cases, the force–deflection curve depends not only on the elastic properties of the beam but also on the self-weight and membrane forces, requiring sophisticated data processing to extract intrinsic material and structural properties. For example, Fig. 12A presents the FEM results of the three-point bending test for a baseline case with a beam length of 4 mm. When self-weight is not considered, the force–deflection curve exhibits an initial linear regime at small deflections, the slope of which can be used to extract the flexural rigidity of the beam. As the ratio of deflection $\delta$ to total thickness $H_{\text{tot}}$ exceeds 0.3, significant geometric nonlinearity arises due to membrane stress. When self-weight is included, the initial $\delta/H_{\text{tot}}$ prior to the application of the point load already exceeds 0.3, placing the entire force–deflection response within the nonlinear regime. Similar nonlinear behavior is widely observed in drumhead indentation tests of 2D materials, where the large deflection and unknown initial membrane stress necessitates complex post-processing and often results in reduced measurement accuracy (Rao and Lu, 2024). Therefore, in scenarios where self-weight induces substantial nonlinearity, the wrinkling-based method offers a simpler and more reliable approach for characterizing the flexural rigidity of laminated beams.

We propose a rule of thumb for determining whether the three-point bending test is applicable: first, calculate the maximum deflection induced by the self-weight, normalized by the total beam thickness, while neglecting geometric nonlinearity. If the normalized deflection exceeds 0.3 (black dashed line in Fig. 12), it is considered large and the three-point bending test is considered inappropriate. As illustrated in Fig. 12, the normalized deflection increases with beam length. For our SU8-PDMS-SU8 system, the wrinkle test is preferred for beams larger than 3 mm.

## 5. Conclusion

In this study, we propose the use of wrinkling on soft substrate as a simple yet effective approach to determine the flexural rigidity of ultrathin laminated beams with shear-lag and present the corresponding analytical framework. The model agrees well with the experimental measurements performed on an SU-8/PDMS/SU-8 trilayer bonded to a soft VHB tape. A systematic parameter study demonstrates that shear-lag theory is governed by the dimensionless shear-lag number and bonded by the Euler–Bernoulli beam theory and the frictionless interface model. Additionally, we make a comparison between the wrinkling test and the standard three-point bending test, and propose a criterion for determining when the wrinkle test is more suited.

## CRediT authorship contribution statement

**Zheliang Wang:** Writing – review & editing, Writing – original draft, Methodology, Investigation, Formal analysis, Conceptualization. **Xinyi Lin:** Writing – review & editing, Writing – original draft, Investigation, Formal analysis, Data curation. **Jia Liu:** Supervision, Project administration, Funding acquisition. **Nanshu Lu:** Writing – review & editing, Project administration, Funding acquisition, Conceptualization.

## Declaration of competing interest

The authors declare that they have no known competing financial interests or personal relationships that could have appeared to influence the work reported in this paper.

## Acknowledgments

This work is supported by the NSF EFRI Award #2422348. The authors thank Foad Vashahi and Paul Le Floch at Axoft, Inc. for providing Fig. 1(B). We dedicate this work to the special issue honoring Prof. Zhigang Suo's 60th birthday. We express our heartfelt gratitude to Zhigang for his inspiring mentorship and visionary contributions to the fields of thin-film mechanics, flexible electronics, and soft matter. We wish Zhigang continued health, happiness, and many more groundbreaking contributions in the years to come.

## Appendix A. Relative energy contribution

In this section, we treat $\epsilon_0$ as a constant. Based on Eq. (25), we can write the axial displacements in the stiff layers in the form of:

$$\mathbf{u} = 2\sqrt{\epsilon_0}\sin(kx)\,\tilde{\mathbf{u}}, \tag{A.1}$$

where $\tilde{\mathbf{u}} = [\tilde{u}_1, \tilde{u}_3, \ldots, \tilde{u}_{2N+1}]^T$ is a vector independent of x. Substituting Eq. (A.1) into Eq. (22), the total beam energy for shear-lag beam theory can be rewritten as:

$$\begin{aligned} U_{\text{beam}}(\tilde{\mathbf{u}}, k) &= f_1(\tilde{\mathbf{u}})\,k^2 + f_2(\tilde{\mathbf{u}}). \\ f_1(\tilde{\mathbf{u}}) &= \epsilon_0 \sum_{k=1}^{k=N+1} \left[\overline{EI}_{2k-1} + \overline{EA}_{2k-1}\tilde{u}_{2k-1}^2\right] \\ f_2(\tilde{\mathbf{u}}) &= \epsilon_0 \sum_{k=1}^{k=N} \frac{G_{2k}}{h_{2k}} \left(\tilde{u}_{2k+1} - \tilde{u}_{2k-1} - h_{2k} - \frac{1}{2}h_{2k-1} - \frac{1}{2}h_{2k+1}\right)^2 \end{aligned} \tag{A.2}$$

where $f_1(\tilde{\mathbf{u}}) = U_{\text{beam}}^{\text{bend}} + U_{\text{beam}}^{\text{stretch}}$ is the bending and stretching energy in the stiff layers, and $f_2(\tilde{\mathbf{u}}) = U_{\text{beam}}^{\text{shear}}$ is the shear energy in the soft layers. The governing equation of the shear-lag beam theory (Eq. (23)) is equivalent to:

$$\frac{\partial U_{\text{beam}}(\tilde{\mathbf{u}}, k)}{\partial \tilde{\mathbf{u}}} = \mathbf{0}, \tag{A.3}$$

which is an implicit equation that prescribes $\tilde{\mathbf{u}}$ as a function of $k$. As discussed in the method section, the wavelength $k$ is obtained by minimizing the total energy with respect to $k$:

$$\begin{aligned} 0 &= \frac{\mathrm{d}U_{\text{tot}}}{\mathrm{d}k} \\ &= \frac{\mathrm{d}U_{\text{sub}}}{\mathrm{d}k} + \frac{\mathrm{d}U_{\text{beam}}(\tilde{\mathbf{u}}, k)}{\mathrm{d}k} \\ &= -\frac{2E_s\epsilon_0}{3k^2} + \frac{\partial U_{\text{beam}}(\tilde{\mathbf{u}}, k)}{\partial k} + \frac{\partial U_{\text{beam}}(\tilde{\mathbf{u}}, k)}{\partial \tilde{\mathbf{u}}}\frac{\partial \tilde{\mathbf{u}}}{\partial k} \\ &= -\frac{2E_s\epsilon_0}{3k^2} + 2k f_1(\tilde{\mathbf{u}}). \end{aligned} \tag{A.4}$$

The simplification utilized the condition of Eq. (A.3). We can further rewrite the equation in terms of energy contribution:

$$U_{\text{sub}} = \frac{2E_s\epsilon_0}{3k} = 2f_1(\tilde{\mathbf{u}})k^2 = 2(U_{\text{beam}}^{\text{bend}} + U_{\text{beam}}^{\text{stretch}}), \tag{A.5}$$

which means that the substrate energy is always two times of the bending energy and the stretching energy in the stiff layers of the laminated beams.

## Appendix B. The equivalent flexural rigidity

The intrinsic definition of flexural rigidity $D$ is the ratio of the internal bending moment $M$ to the local curvature $\kappa$, which is equivalent to the following.

$$U_{\text{beam}}^{\text{bend}} + U_{\text{beam}}^{\text{stretch}} = \frac{1}{\lambda}\int_0^{\lambda} \frac{1}{2} D\kappa^2 dx = \epsilon_0 k^2 D \tag{B.1}$$

Substituting Eq. (A.5), we have:

$$D = \frac{f_1(\tilde{\mathbf{u}})k^2}{\epsilon_0 k^2} = \frac{E_s\epsilon_0}{3k} = \frac{E_s}{3}\left(\frac{\lambda}{2\pi}\right)^3. \tag{B.2}$$

## Appendix C. Supplementary data

Supplementary material related to this article can be found online at https://doi.org/10.1016/j.jmps.2025.106172.

## Data availability

Data will be made available on request.

## References


Bae, J., Ouchi, T., Hayward, R.C., 2015. Measuring the elastic modulus of thin polymer sheets by elastocapillary bending. ACS Appl. Mater. & Interfaces 7 (27), 14734–14742.

Beams, J., 1959. Mechanical properties of thin film of gold and silver. Struct. Prop. Thin Film.

Begley, M.R., Mackin, T.J., 2004. Spherical indentation of freestanding circular thin films in the membrane regime. J. Mech. Phys. Solids 52 (9), 2005–2023.

Chen, W., Gui, X., Yang, L., Zhu, H., Tang, Z., 2019. Wrinkling of two-dimensional materials: methods, properties and applications. Nanoscale Horizons 4 (2), 291–320.

Chen, X., Hutchinson, J.W., 2004. Herringbone buckling patterns of compressed thin films on compliant substrates. J. Appl. Mech. 71 (5), 597–603.

Chen, Y., Liu, H., Pang, K., Zhang, C., Qin, H., Xu, Z., Liu, Y., 2023. Bending deformable tension-shear model for nacre-like composites. J. Mech. Phys. Solids 171, 105132.

Chung, J.Y., Nolte, A.J., Stafford, C.M., 2011. Surface wrinkling: a versatile platform for measuring thin-film properties. Adv. Mater. 23 (3), 349–368.

Cox, H., 1952. The elasticity and strength of paper and other fibrous materials. Br. J. Appl. Phys. 3 (3), 72.

Gao, X.-L., Li, K., 2005. A shear-lag model for carbon nanotube-reinforced polymer composites. Int. J. Solids Struct. 42 (5–6), 1649–1667.

Geiger, S., Michon, J., Liu, S., Qin, J., Ni, J., Hu, J., Gu, T., Lu, N., 2020. Flexible and stretchable photonics: The next stretch of opportunities. ACS Photonics 7 (10), 2618–2635. http://dx.doi.org/10.1021/acsphotonics.0c00983.

Groenewold, J., 2001. Wrinkling of plates coupled with soft elastic media. Phys. A 298 (1–2), 32–45.

Haque, M.A., Saif, M.T.A., 2003. A review of MEMS-based microscale and nanoscale tensile and bending testing. Exp. Mech. 43, 248–255.

He, J., Cao, L., Cui, J., Fu, G., Jiang, R., Xu, X., Guan, C., 2024. Flexible energy storage devices to power the future. Adv. Mater. 36 (4), 2306090.

Hemker, K.J., Sharpe Jr., W.N., 2007. Microscale characterization of mechanical properties. Annu. Rev. Mater. Res. 37 (1), 93–126.

Huang, Z., He, Z., Zhu, Y., Wu, H., 2023. A general theory for the bending of multilayer van der Waals materials. J. Mech. Phys. Solids 171, 105144.

Huang, Z., Hong, W., Suo, Z., 2005. Nonlinear analyses of wrinkles in a film bonded to a compliant substrate. J. Mech. Phys. Solids 53 (9), 2101–2118.

Hui, Z., Zhang, L., Ren, G., Sun, G., Yu, H.-D., Huang, W., 2023. Green flexible electronics: natural materials, fabrication, and applications. Adv. Mater. 35 (28), 2211202.

Jang, H., Sel, K., Kim, E., Kim, S., Yang, X., Kang, S., Ha, K.-H., Wang, R., Rao, Y., Jafari, R., et al., 2022. Graphene e-tattoos for unobstructive ambulatory electrodermal activity sensing on the palm enabled by heterogeneous serpentine ribbons. Nat. Commun. 13 (1), 6604.

Kim, D.-H., Viventi, J., Amsden, J.J., Xiao, J., Vigeland, L., Kim, Y.-S., Blanco, J.A., Panilaitis, B., Frechette, E.S., Contreras, D., et al., 2010. Dissolvable films of silk fibroin for ultrathin conformal bio-integrated electronics. Nat. Mater. 9 (6), 511–517.

Le Floch, P., Zhao, S., Liu, R., Molinari, N., Medina, E., Shen, H., Wang, Z., Kim, J., Sheng, H., Partarrieu, S., et al., 2024. 3D spatiotemporally scalable in vivo neural probes based on fluorinated elastomers. Nature Nanotechnology 19 (3), 319–329.

Lee, G.J., Choi, C., Kim, D.-H., Song, Y.M., 2018. Bioinspired artificial eyes: Optic components, digital cameras, and visual prostheses. Adv. Funct. Mater. 28 (24), 1705202. http://dx.doi.org/10.1002/adfm.201705202, arXiv:https://onlinelibrary.wiley.com/doi/pdf/10.1002/adfm.201705202, URL https://onlinelibrary.wiley.com/doi/abs/10.1002/adfm.201705202.

Lee, T.-I., Jo, W., Kim, W., Kim, J.-H., Paik, K.-W., Kim, T.-S., 2019. Direct visualization of cross-sectional strain distribution in flexible devices. ACS Appl. Mater. & Interfaces 11 (14), 13416–13422.

Li, S., Li, R., An, D., Wang, Y., Xu, X., Xue, R., Su, Y., 2022. Bioinspired staggered-array structure design for flexible batteries. Int. J. Solids Struct. 256, 111986.

Li, L., Lin, H., Qiao, S., Zou, Y., Danto, S., Richardson, K., Musgraves, J.D., Lu, N., Hu, J., 2014. Integrated flexible chalcogenide glass photonic devices. Nat. Photonics 8 (8), 643–649.

Li, S., Liu, X., Li, R., Su, Y., 2017. Shear deformation dominates in the soft adhesive layers of the laminated structure of flexible electronics. Int. J. Solids Struct. 110, 305–314.

Li, S., Su, Y., Li, R., 2016. Splitting of the neutral mechanical plane depends on the length of the multi-layer structure of flexible electronics. Proc. R. Soc. A: Math. Phys. Eng. Sci. 472 (2190), 20160087.

Li, H., Tan, P., Rao, Y., Bhattacharya, S., Wang, Z., Kim, S., Gangopadhyay, S., Shi, H., Jankovic, M., Huh, H., et al., 2024. E-Tattoos: Toward functional but imperceptible interfacing with human skin. Chem. Rev. 124 (6), 3220–3283.

Liu, H., Chen, Y., Liu, L., Liu, Y., Zheng, Q., Homogenization of Two-Dimensional Materials Integrating Monolayer Bending and Surface Layer Effects, Available at SSRN 4799329.

Liu, S., Rao, Y., Jang, H., Tan, P., Lu, N., 2022. Strategies for body-conformable electronics. Matter 5 (4), 1104–1136. http://dx.doi.org/10.1016/j.matt.2022.02.006.

Luo, Y., Abidian, M.R., Ahn, J.-H., Akinwande, D., Andrews, A.M., Antonietti, M., Bao, Z., Berggren, M., Berkey, C.A., Bettinger, C.J., Chen, J., Chen, P., Cheng, W., Cheng, X., Choi, S.-J., Chortos, A., Dagdeviren, C., Dauskardt, R.H., Di, C.-a., Dickey, M.D., Duan, X., Facchetti, A., Fan, Z., Fang, Y., Feng, J., Feng, X., Gao, H., Gao, W., Gong, X., Guo, C.F., Guo, X., Hartel, M.C., He, Z., Ho, J.S., Hu, Y., Huang, Q., Huang, Y., Huo, F., Hussain, M.M., Javey, A., Jeong, U., Jiang, C., Jiang, X., Kang, J., Karnaushenko, D., Khademhosseini, A., Kim, D.-H., Kim, I.-D., Kireev, D., Kong, L., Lee, C., Lee, N.-E., Lee, P.S., Lee, T.-W., Li, F., Li, J., Liang, C., Lim, C.T., Lin, Y., Lipomi, D.J., Liu, J., Liu, K., Liu, N., Liu, R., Liu, Y., Liu, Y., Liu, Z., Liu, Z., Loh, X.J., Lu, N., Lv, Z., Magdassi, S., Malliaras, G.G., Matsuhisa, N., Nathan, A., Niu, S., Pan, J., Pang, C., Pei, Q., Peng, H., Qi, D., Ren, H., Rogers, J.A., Rowe, A., Schmidt, O.G., Sekitani, T., Seo, D.-G., Shen, G., Sheng, X., Shi, Q., Someya, T., Song, Y., Stavrinidou, E., Su, M., Sun, X., Takei, K., Tao, X.-M., Tee, B.C.K., Thean, A.V.-Y., Trung, T.Q., Wan, C., Wang, H., Wang, J., Wang, M., Wang, S., Wang, T., Wang, Z.L., Weiss, P.S., Wen, H., Xu, S., Xu, T., Yan, H., Yan, X., Yang, H., Yang, L., Yang, S., Yin, L., Yu, C., Yu, G., Yu, J., Yu, S.-H., Yu, X., Zamburg, E., Zhang, H., Zhang, X., Zhang, X., Zhang, X., Zhang, Y., Zhang, Y., Zhao, S., Zhao, X., Zheng, Y., Zheng, Y.-Q., Zheng, Z., Zhou, T., Zhu, B., Zhu, M., Zhu, R., Zhu, Y., Zhu, Y., Zou, G., Chen, X., 2023. Technology roadmap for flexible sensors. ACS Nano 17 (6), 5211–5295. http://dx.doi.org/10.1021/acsnano.2c12606, PMID: 36892156.

Maner, K.C., Begley, M.R., Oliver, W.C., 2004. Nanomechanical testing of circular freestanding polymer films with sub-micron thickness. Acta Mater. 52 (19), 5451–5460.

Mazzotta, A., Carlotti, M., Mattoli, V., 2021. Conformable on-skin devices for thermo-electro-tactile stimulation: Materials, design, and fabrication. Mater. Adv. 2 (6), 1787–1820.

Qin, H., Yan, Y., Liu, H., Liu, J., Zhang, Y.-W., Liu, Y., 2020. Modified timoshenko beam model for bending behaviors of layered materials and structures. Extrem. Mech. Lett. 39, 100799.

Rao, Y., Lu, N., 2024. Effects of adhesive and frictional contacts on the nanoindentation of two-dimensional material drumheads. J. Mech. Phys. Solids 105828.

Reissner, E., 1946. Analysis of shear lag in box beams by the principle of minimum potential energy. Quart. Appl. Math. 4 (3), 268–278.

Shen, X., Wei, Y., Liu, Y., 2024. Unlocking slip-mediated bending in multilayers: Efficient modeling and solutions with high precision and simplicity. Int. J. Solids Struct. 302, 112971.

Shi, Y., Rogers, J.A., Gao, C., Huang, Y., 2014. Multiple neutral axes in bending of a multiple-layer beam with extremely different elastic properties. J. Appl. Mech. 81 (11), 114501.

Song, J., Jiang, H., Liu, Z., Khang, D., Huang, Y., Rogers, J., Lu, C., Koh, C., 2008. Buckling of a stiff thin film on a compliant substrate in large deformation. Int. J. Solids Struct. 45 (10), 3107–3121.

Song, Y., Min, J., Gao, W., 2019. Wearable and implantable electronics: Moving toward precision therapy. ACS Nano 13 (11), 12280–12286. http://dx.doi.org/10.1021/acsnano.9b08323, PMID: 31725255.

Stafford, C.M., Harrison, C., Beers, K.L., Karim, A., Amis, E.J., VanLandingham, M.R., Kim, H.-C., Volksen, W., Miller, R.D., Simonyi, E.E., 2004. A buckling-based metrology for measuring the elastic moduli of polymeric thin films. Nat. Mater. 3 (8), 545–550.

Standard, A., 1997. Standard test methods for flexural properties of unreinforced and reinforced plastics and electrical insulating materials. ASTM D790. In: Annual Book of ASTM Standards.

Standard, I., Iso, B., 2019. Plastics—Determination of Flexural Properties. ISO Geneva, Switzerland.

Su, Y., Li, S., Li, R., Dagdeviren, C., 2015. Splitting of neutral mechanical plane of conformal, multilayer piezoelectric mechanical energy harvester. Appl. Phys. Lett. 107 (4), 041905.

Sunwoo, S.-H., Ha, K.-H., Lee, S., Lu, N., Kim, D.-H., 2021. Wearable and implantable soft bioelectronics: device designs and material strategies. Annu. Rev. Chem. Biomol. Eng. 12, 359–391.

Timoshenko, S., Woinowsky-Krieger, S., 1959. Theory of plates and shells.

Uzun, M., Anand, S.C., Shah, T., 2016. A novel approach for designing nonwoven hybrid wound dressings: Processing and characterisation. J. Ind. Text. 45 (6), 1383–1398.

Vallem, V., Sargolzaeiaval, Y., Ozturk, M., Lai, Y.-C., Dickey, M.D., 2021. Energy harvesting and storage with soft and stretchable materials. Adv. Mater. 33 (19), 2004832.

Vlassak, J., Nix, W., 1992. A new bulge test technique for the determination of Young's modulus and Poisson's ratio of thin films. J. Mater. Res. 7 (12), 3242–3249.

Wang, L., Lu, N., 2016. Conformability of a thin elastic membrane laminated on a soft substrate with slightly wavy surface. J. Appl. Mech. 83 (4), 041007.

Wang, Y., Shao, B., Song, J., Hong, W., Guo, C.F., 2024b. Mechanical tester driven by surface tension. Nano Lett. 24 (13), 4012–4019.

Wang, Z., Sheng, H., Lin, X., Rao, Y., Liu, J., Lu, N., 2024a. A shear-lag model for laminated beams with extreme modulus mismatch between layers. Mech. Mater. 188, 104844.

Whiting, R., Angadi, M., 1990. Young's modulus of thin films using a simplified vibrating reed method. Meas. Sci. Technol. 1 (7), 662.

Xiang, Y., Chen, X., Vlassak, J.J., 2005. Plane-strain bulge test for thin films. J. Mater. Res. 20 (9), 2360–2370.

Xiong, P., Sun, B., Sakai, N., Ma, R., Sasaki, T., Wang, S., Zhang, J., Wang, G., 2020. 2D superlattices for efficient energy storage and conversion. Adv. Mater. 32 (18), 1902654.

Yang, J.C., Mun, J., Kwon, S.Y., Park, S., Bao, Z., Park, S., 2019. Electronic skin: Recent progress and future prospects for skin-attachable devices for health monitoring, robotics, and prosthetics. Adv. Mater. 31 (48), 1904765. http://dx.doi.org/10.1002/adma.201904765, URL https://onlinelibrary.wiley.com/doi/abs/10.1002/adma.201904765.

Zhang, Z., Liu, P., Song, Y., Hou, Y., Xu, B., Liao, T., Zhang, H., Guo, J., Sun, Z., 2022. Heterostructure engineering of 2D superlattice materials for electrocatalysis. Adv. Sci. 9 (35), 2204297.

Zhao, Z., Liu, K., Liu, Y., Guo, Y., Liu, Y., 2022. Intrinsically flexible displays: key materials and devices. Natl. Sci. Rev. 9 (6), nwac090. http://dx.doi.org/10.1093/nsr/nwac090, arXiv:https://academic.oup.com/nsr/article-pdf/9/6/nwac090/44063383/nwac090.pdf.

Zhao, H., Yang, Z., Guo, L., 2018. Nacre-inspired composites with different macroscopic dimensions: strategies for improved mechanical performance and applications. NPG Asia Mater. 10 (4), 1–22.